Optical Engineering

OpticalEngineering.SPIEDigitalLibrary.org

View-dependent geometric calibration for offset flat-panel cone beam computed tomography systems

Van-Giang Nguyen

SPIE.

Van-Giang Nguyen, "View-dependent geometric calibration for offset flat-panel cone beam computed tomography systems," *Opt. Eng.* **55**(4), 043102 (2016), doi: 10.1117/1.OE.55.4.043102.

Optical Engineering 55(4), 043102 (April 2016)

View-dependent geometric calibration for offset flat-panel cone beam computed tomography systems

Van-Giang Nguyen*
Le Quy Don Technical University, Department of Information Systems, 236 Hoang Quoc Viet, Bac Tu Liem, Ha Noi, Vietnam

Abstract. Geometric parameters that define the geometry of imaging systems are crucial for image reconstruction and image quality in x-ray computed tomography (CT). The problem of determining geometric parameters for an offset flat-panel cone beam CT (CBCT) system, a recently introduced modality with a large field of view, with the assumption of an unstable mechanism and geometric parameters that vary in each view, is considered. To accurately and rapidly find the geometric parameters for each projection view, we use the projection matrix method and design a dedicated phantom that is partially visible in all projection views. The phantom consists of balls distributed symmetrically in a cylinder to ensure the inclusion of the phantom in all views, and a large portion of the phantom is covered in the projection image. To efficiently use calibrated geometric information in the reconstruction process and get rid of approximation errors, instead of decomposing the projection matrix into actual geometric parameters that are manually corrected before being used in reconstruction, as in conventional methods, we directly use the projection matrix and its pseudo-inverse in projection and backprojection operations of reconstruction algorithms. The experiments illustrate the efficacy of the proposed method with a real offset flat-panel CBCT system in dental imaging. [DOI: 10.1117/1.OE.55.4.043102]

Keywords: geometric calibration; perspective geometry; computed tomography; offset flat-panel cone beam computed tomography; projection matrix.

Paper 151732 received Dec. 5, 2015; accepted for publication Mar. 15, 2016; published online Apr. 12, 2016.

1 Introduction

X-ray computed tomography (CT) is an imaging technique that provides anatomical information about the object and is now a major imaging modality in medicine. In CT imaging, the images shown to the doctor are not directly acquired from the scanner but reconstructed from projection data (which were generated by the detector of the scanner).[1] Many algorithms have been proposed to reconstruct CT images (a.k.a. cross-sectional slices) from projection data, where some have the potential to significantly reduce the radiation dose, while the others can rapidly provide the result.

One major requirement in all reconstruction algorithms in CT imaging is knowledge about the geometry of the imaging system. Minor errors in geometric parameters result in major artifacts in reconstruction.[2] In ideal conditions, one can assume that the imaging system is perfectly manufactured and the geometric parameters are highly accurate before shifting to practical usage. However, due to unwanted factors when shifting the scanner and the degradation of the system from time and human factors, the precalculated geometric parameters are less reliable. Those facts lead to the requirement of a method to automatically measure geometric parameters of the CT scanner.

Existing geometric calibration methods can be classified into two categories: phantom-based (offline) methods[3–5] and phantom-less (online) methods.[6–9] In phantom-based methods, the projection of a calibration phantom, which consists of several steel balls, is first carried and followed by computation to estimate geometric parameters. The phantom-based calibration method has the following steps: (i) measure the projected location of balls (and their center points) in the projection image; (ii) set up equations that relate the found locations in step (i) and the predefined position of the centers of balls in the phantom; and (iii) solve the equations to find geometric parameters. If a highly accurate calibration phantom is available, phantom-based methods achieve the most accurate geometrical parameters.[5]

In phantom-less methods, the geometric parameters are calculated directly from the projection images without the use of a calibration phantom. The calibration process is mostly performed concurrently with reconstruction. The computation relies on a complex optimization whose objective function is in the projection domain[6] or in the reconstructed volume domain.[9–12] (see Ref. 8 for more information). However, these methods suffer from expensive computation loads as well as less accurate results in comparison with phantom-based methods, though they have the advantage of not using calibration phantoms.

Regarding their abilities, geometric calibration methods can be classified into view-independent and view-dependent methods. The first ones assume that the system is mechanically stable and a large set of geometric parameters are fixed in all views. Meanwhile, the latter ones are met in practice where the geometric parameters vary in each view. This is due to the imperfect design and unstable mechanism of the scanner and the imbalance of the suspension arm holding the x-ray source and detector, as well as the nonsymmetry of the scanner, especially in mid- and low-end ones with flat-panel detectors.

*Address all correspondence to: Van-Giang Nguyen, E-mail: giangnv@mta.edu.vn

0091-3286/2016/$25.00

Among methods to estimate geometric parameters for each view, the projection matrix-based method is the most widely used due to its fast computation and reliable results. With accurate calibration phantom, the projection matrix method can provide subdetector unit and subdegree angular accuracy. It has been shown to provide state-of-the-art results (in comparison with other existing methods) in C-arm CT, micro-CT, and digital tomosynthesis systems.

Offset flat-panel CBCT systems are recently introduced CBCT systems with applications in multimodality systems (such as PET/CT and SPECT/CT) and dental imaging. However, due to their imbalanced mechanism, geometric calibration for them is difficult and yet to be thoroughly considered. In this work, we develop a projection matrix-based method for calibrating offset flat-panel CBCT systems. The new method comes with a dedicated phantom for offset flat-panel CBCT systems as well as a new technique to prevent numerical errors due to approximations, which are usually involved in conventional projection matrix methods. In particular, instead of decomposing the projection matrix into subsequent geometric elements, which are manually corrected before using in reconstruction, we directly use the projection matrix and its pseudo-inverse matrix in the reconstruction process.

The remainder of this paper is organized as follows. Section 2 presents a projection matrix-based calibration method, imaging geometry, and calibration phantom for offset flat-panel CBCT systems. This section also presents a method to improve the accuracy of calibration via the use of the projection matrix and its inverse (rather than actual geometric parameters) in reconstruction. Section 3 presents our experimental studies. Section 4 presents discussion and the conclusion of this article.

2 Methods

2.1 *View-Dependent Projection Matrix-Based Calibration Method*

In x-ray imaging systems, given a point source (x-ray source) and a two-dimensional (2-D) detector, a point (x, y, z) in object coordinates will be projected onto the detector at a point coordinated at (u, v) in detector coordinates (see Fig. 1).

The mathematical relationship between two points is represented via the following equation, which is a mapping between two coordinates [a three-dimensional (3-D) point in object coordinates and a 2-D point in detector coordinates]:

$$[uw, vw, w]^T = \mathbf{P}[x, y, z, 1]^T, \tag{1}$$

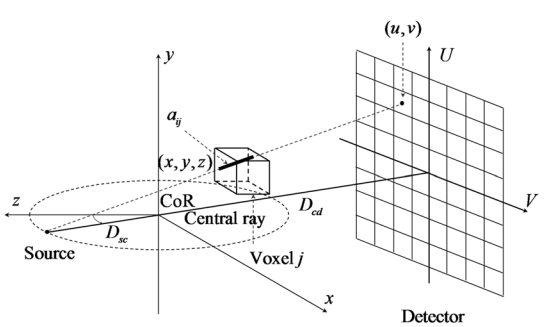

Fig. 1 Cone-beam CT geometry and its 3-D to 2-D projection.

where $\mathbf{P}$ is a 3×4 projection matrix and w is a weighting factor.

The projection matrix $\mathbf{P}$ can be factorized as

$$\mathbf{P} = \mathbf{K}[\mathbf{R}|\mathbf{t}], \tag{2}$$

where $\mathbf{K}$ is a 3×3 intrinsic matrix, $\mathbf{R}$ is a 3×3 rotation matrix, and $\mathbf{t}$ is a 3×1 translation vector.

$\mathbf{K}$ contains intrinsic geometric information about the imaging system and has the following form:

$$\mathbf{K} = \begin{bmatrix} \frac{f}{p_u} & \frac{f}{p_u \tan \alpha} & u_0 \\ 0 & \frac{f}{p_v \sin \alpha} & v_0 \\ 0 & 0 & 1 \end{bmatrix}, \tag{3}$$

where f is the distance from the source to the detector; p_u, p_v represents the width and height of the detector element (detector bin), respectively; α is the angle formed by two axes of the detector bin (which is usually assumed to be exactly 90 deg in other works, but this is not the case in practice); and (u_0, v_0) is the coordinate of the central ray (the ray starting from source and is perpendicular to the detector) and the detector.

$\mathbf{R}$ is (an orthogonal) rotation matrix $\mathbf{R} = \mathbf{R}_z\mathbf{R}_y\mathbf{R}_x$, where $\mathbf{R}_x$, $\mathbf{R}_y$, $\mathbf{R}_z$ is the rotation matrix around the x, y, and z axes, respectively.

In current practice, once the projection matrix $\mathbf{P}$ is calculated, it will be decomposed into subsequent matrices $\mathbf{K}$, $\mathbf{R}$, and $\mathbf{t}$, from which the actual geometric parameters are extracted. The extraction process involves the use of RQ decomposition and normalizations (see Ref. 4 for details). The calculated values will be compared with the measured values given by measurement techniques (or provided by the manufacturer), and adjustments will be made to each parameter. The adjusted values will later be used in reconstruction. However, the numerical result might not match with predefined assumptions about the system. For example, the $\mathbf{K}$ matrix does not satisfy the preset values of p_u, p_v, and α. The projection matrix $\mathbf{P}$ constructed from the adjusted geometric parameters does not match the one calculated from the calibration process (Sec. 2.3 will discuss this issue in detail).

In order to measure $\mathbf{P}$ in Eq. (1) for each view, we need several pairs of (u_i, v_i) and (x_i, y_i, z_i) with $i = 1, \ldots, N$. To obtain these, a calibration phantom is used. The phantom consists of several steel balls whose centers correspond to (x_i, y_i, z_i) in Eq. (1). The balls are positioned in a cylindrical plastic (or glass) holder. The phantom is designed and manufactured with high accuracy. To find (u_i, v_i), we project the balls onto the detector by illuminating the phantom in the scanner and find the centroids of the ellipses that were projections of balls in the projection data.[4,12] To accurately find the centroids of ellipses, the following steps are used: (i) remove the noise in the projection images using a noise filter; (ii) detect edges using the Canny edge detector; (iii) locate the ellipse centers using a curve-fitting algorithm, which processes the detected edge pixels of the balls to result in centroids.

Given the calibration dataset, which in this case is a group of 3-D points (x_i, y_i, z_i), where $i = 1, \ldots, N$ (where N is the number of balls in the projection view) and their 2-D projected points (u_i, v_i), we can determine the geometric

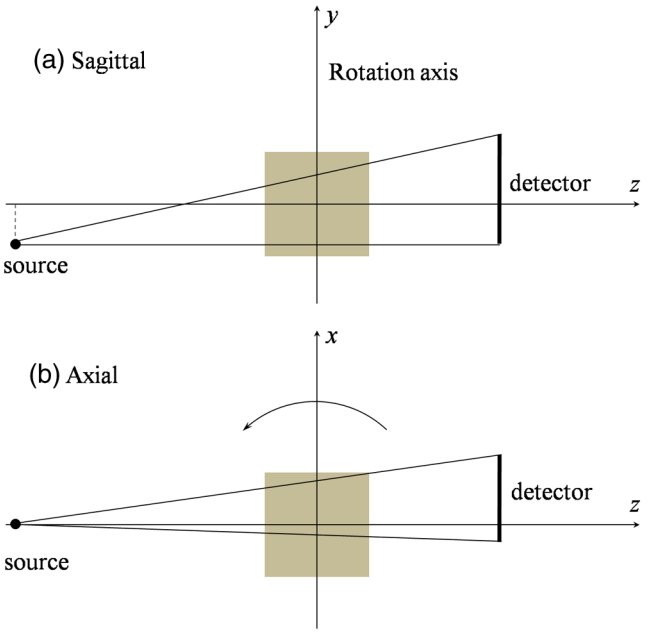

Fig. 2 Illustration of an offset flat-panel CBCT system: (a) sagittal view and (b) axial view.

parameters by solving the linear systems of equations (1) via the singular value decomposition technique or a least square optimization technique such as Levenberg–Marquardt algorithm.[13]

The projection matrix–based calibration method described above is designed to find geometric parameters for each view of a standard CBCT system, where all information about the phantom is captured in a single view. However, to apply it to offset flat-panel CBCT, some issues need to be resolved.

2.2 *Geometric Calibration for Offset Flat-Panel Cone Beam Computed Tomography*

In an offset flat-panel CBCT system, the source–detector axis is positioned offset to the center of rotation so that the field-of-view of a scanner can be enlarged. This extension poses difficulties to reconstruction[14,15] and geometric calibration. In particular, for a given calibration phantom, in each view, the projection image contains projection information about only a portion of the object, as illustrated in Fig. 2.

To calibrate the offset CBCT, in this work, we designed a phantom, which has a structure as illustrated in Fig. 3. The phantom was made with 24 metal balls; each is a sphere with diameter 2 mm. These 24 balls are distributed into two circular shapes with diameters of 110 mm. The distance between two virtual circles is 25 mm. The phantom is designed for an offset CBCT system in dental imaging (Papaya 3D™ scanner from Genoray Co., Ltd., South Korea). The calibration phantom was manufactured with the ball centers positioned at (x_i, y_i, z_i) with $i = 1, \ldots, N$. The phantom was then illuminated using an independent CT system to determine its 3-D CT image. The actual positions of ball centers (x_i, y_i, z_i) were refined according to the results in the 3-D CT image.

To appropriately align the calibration phantom with the rotation center of the scanner so that all projection views contain almost the same structural information about the phantom, we use an additional positioning laser light equipped in the scanner to pinpoint the position to place the calibration phantom. There is no specific requirement for the accuracy of alignment since it has no role in determining the projection matrix or geometric parameters.

Theoretically, to accurately estimate the projection matrix **P**, the number of visible balls in the projection image should not be smaller than 6 (since the projection matrix **P** has 12 elements to be estimated, while each ball yields two equations relating **P** and the ball center). Here, we use 24 balls to stabilize the solution and improve the accuracy in the geometric calibration. The number of balls is chosen and symmetrically distributed so that the overlapping of balls does not show up in the projection image.

To estimate the projection matrix for a projection view, we need two lists sorted in the same order: coordinates of centers of steel balls in the object coordinate (x_i, y_i, z_i) and coordinates of their projection in the projection (detector) coordinate (u_i, v_i) with $i = 1, \ldots, N$. (For the offset flat-panel CBCT system, the number of visible balls in the projection image is less than N, and in our configuration,

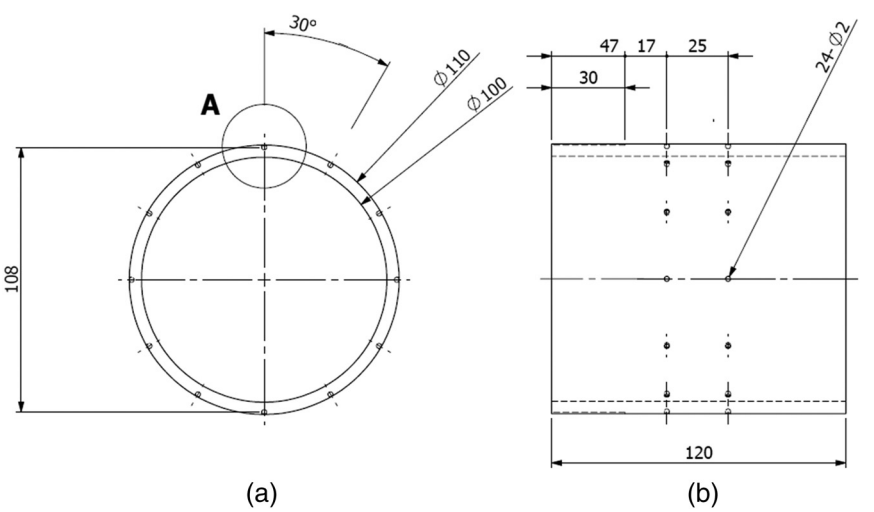

Fig. 3 Structure of the proposed calibration phantom for offset flat-panel CBCT. (a) Axial view; (b) sagittal view.

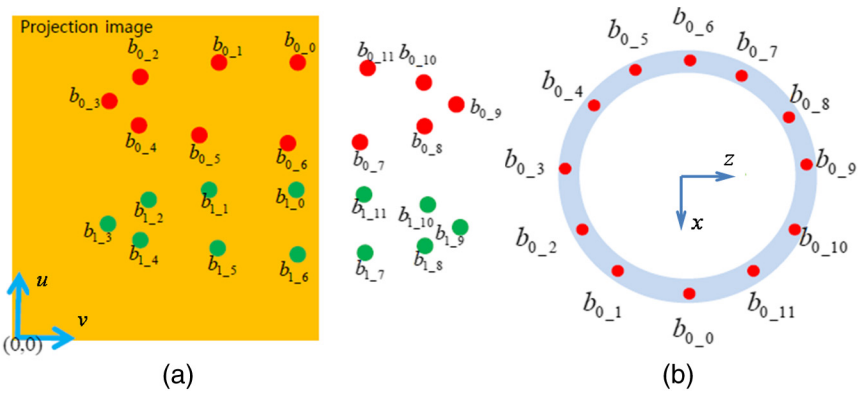

Fig. 4 Illustration of calibration phantom and its projection image: (a) a projection image where only part of phantom is visible and (b) axial view of the calibration phantom. The calibration process requires the coordinates of ball centers in object coordinates (b) and its projection in (a) sorted in the same order.

it varies between 14 and 16.) While we have the first full list of object coordinates (which is known from the design process), the associated one in projection coordinates is difficult to construct since only a few balls are visible in each projection view. In particular, it is difficult to label or match the center of each ball in object coordinates with its corresponding projected center in the projection image (see Fig. 4 for illustration).

To label balls in the projection image, we first separate the projection balls into two groups, upper and lower. Then, we find the centers of all ellipses using the ellipse fitting technique. From the calculated centers of ellipses (a.k.a. the ball centers), we calculate the virtual center of the ball centers by simple averaging. The angles between the line connecting each ball center and the virtual center and the horizontal axis crossing the virtual center will be measured. The balls are then ordered and labeled according to the measured angles. The resulting list is now matched with the one in object coordinates. Figure 5 illustrates our method to label balls in the projection image.

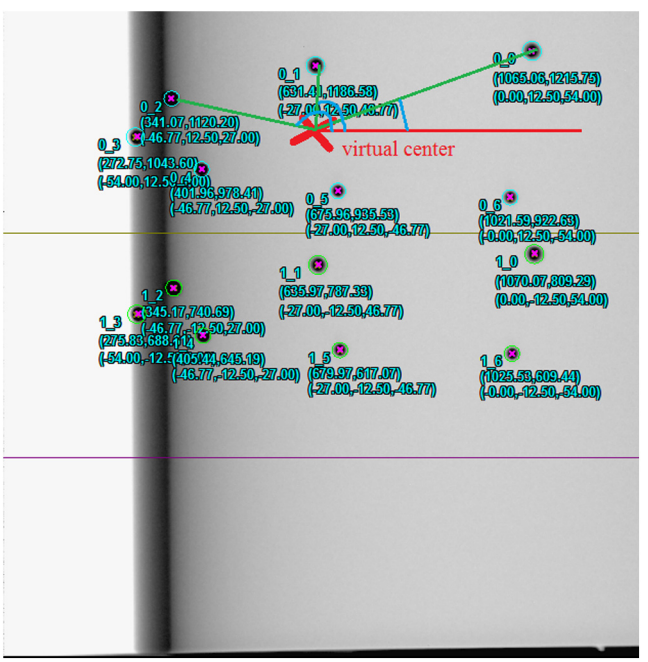

Fig. 5 Method to label balls in projection image. For each group, the virtual center (large cross sign) is first determined, then the angle of each ball with the horizontal axis crossing the virtual center will be calculated and used to determine its label. The small cross sign on each ball indicates the centroid calculated using the ellipse fitting technique. The final goal is to assign ball centers in the projection image to the 3-D ones in object coordinates.

2.3 *Errors due to the Extraction of Geometric Parameters from Projection matrix*

In both conventional full-beam CBCT and offset flat-panel CBCT, the intermediate output of the geometrical calibration process is the projection matrix **P**. This matrix is then decomposed into subsequent elements. In particular, once the projection matrix **P** is computed, we will get the intrinsic matrix **K**, rotation matrix **R**, and translation vector **t**.

In the conventional methods (which are widely used in practice), after estimating **P**, and then **R**, **K**, and **t**, the actual geometric parameters embedded in **R**, **K**, and **t** are calculated via decomposition techniques and might be followed by manual corrections. The decompositions involve preset constraints (some parameters are known beforehand) and approximations that might result in numerical errors in the modeling projection image.

We validated this fact by conducting perturbation analysis using a software simulation. The modeled system had $f = 620$ mm, distance from source to rotation center $= 418$ mm, $\theta_x = \theta_y = 0$, and rotation angle $\theta_z = 22.86°, 45.71°, 67.75°, 89.80°$ for four different views. The experiment consisted of the following steps:

a. Generate ground-truth values of geometric parameters, denoted by $\mathbf{G}^{\text{true}}$, and the ground-truth values of ball centers in the phantom $(x_i, y_i, z_i)^{\text{true}}$ with $i = 1, \ldots, N$ (its values matched with the phantom, as described in Sec. 2.2). The two axes of the detector were perfectly perpendicular to each other.

b. Calculate the ground-truth projection matrix $\mathbf{P}^{\text{true}}$ from $\mathbf{G}^{\text{true}}$.

c. Calculate the projection of $(x_i, y_i, z_i)^{\text{true}}$ with $i = 1, \ldots, N$ in the detector using $\mathbf{P}^{\text{true}}$ and denote the result as $(u_i, v_i)^{\text{true}}$.

d. Model the imperfect placement of $(x_i, y_i, z_i)^{\text{true}}$ in the calibration phantom by adding Gaussian noise

Table 1 Mean and standard deviation of error distance calculated from 50 noise trials.

Ball (i)	View 1		View 2		View 3		View 4	
	d_i^A	d_i^B	d_i^A	d_i^B	d_i^A	d_i^B	d_i^A	d_i^B
1	0.35 ± 0.17	1.13 ± 0.79	0.29 ± 0.14	0.84 ± 0.54	0.33 ± 0.17	0.77 ± 0.59	0.44 ± 0.23	1.19 ± 0.88
2	0.34 ± 0.18	1.18 ± 0.82	0.33 ± 0.16	0.93 ± 0.62	0.37 ± 0.20	0.89 ± 0.65	0.42 ± 0.21	1.18 ± 0.90
3	0.35 ± 0.20	1.29 ± 0.91	0.38 ± 0.17	0.99 ± 0.67	0.35 ± 0.20	0.92 ± 0.60	0.37 ± 0.20	1.13 ± 0.90
4	0.36 ± 0.18	1.32 ± 0.94	0.34 ± 0.19	0.96 ± 0.67	0.36 ± 0.17	0.91 ± 0.56	0.46 ± 0.19	1.34 ± 1.11
5	0.49 ± 0.26	1.33 ± 0.92	0.32 ± 0.18	0.85 ± 0.55	0.34 ± 0.18	0.70 ± 0.46	0.39 ± 0.21	1.04 ± 0.78
6	0.39 ± 0.21	1.51 ± 1.10	0.29 ± 0.13	1.14 ± 0.76	0.34 ± 0.15	1.14 ± 0.76	0.41 ± 0.23	1.65 ± 1.35
7	0.34 ± 0.17	1.68 ± 1.27	0.33 ± 0.16	1.29 ± 0.90	0.35 ± 0.18	1.29 ± 0.85	0.42 ± 0.21	1.68 ± 1.39
8	0.35 ± 0.19	1.89 ± 1.45	0.38 ± 0.18	1.38 ± 1.00	0.33 ± 0.19	1.30 ± 0.84	0.39 ± 0.22	1.59 ± 1.34
9	0.38 ± 0.20	1.98 ± 1.50	0.36 ± 0.18	1.32 ± 0.97	0.33 ± 0.19	1.22 ± 0.77	0.47 ± 0.27	1.73 ± 1.43
10	0.57 ± 0.28	1.61 ± 1.14	0.30 ± 0.14	1.05 ± 0.68	0.34 ± 0.17	0.96 ± 0.64	0.34 ± 0.17	1.44 ± 1.19

to it and denote the result as $(x_i, y_i, z_i)^{\text{noisy}}$ with $i = 1, \ldots, N$.

e. Calculate the projection of $(x_i, y_i, z_i)^{\text{noisy}}$ in the detector using $\mathbf{P}^{\text{true}}$, followed by adding Gaussian noise to the resulting projection (to model the error in estimating ball centers from the projection) and denote the result as $(u_i, v_i)^{\text{noisy}}$ with $i = 1, \ldots, N$.

f. Estimate the projection matrix from $(x_i, y_i, z_i)^{\text{noisy}}$ and $(u_i, v_i)^{\text{noisy}}$ with $i = 1, \ldots, N$ and denote the result as $\mathbf{P}^{\text{est}}$.

g. Calculate the reprojection of $(x_i, y_i, z_i)^{\text{true}}$ in the detector using $\mathbf{P}^{\text{est}}$ and denote the result as $(u_i, v_i)^{\text{A}}$. Measure the distance d_i^A from $(u_i, v_i)^{\text{A}}$ to $(u_i, v_i)^{\text{true}}$ with $i = 1, \ldots, N$.

h. Decompose $\mathbf{P}^{\text{est}}$ to get geometric parameters $\mathbf{G}^{\text{est}}$ with the constraint of the detector having perpendicular axes (this constraint was known beforehand). Calculate the projection of $(x_i, y_i, z_i)^{\text{true}}$ in the detector using $\mathbf{G}^{\text{est}}$ and denote the result as $(u_i, v_i)^{\text{B}}$. Measure the distance d_i^B from $(u_i, v_i)^{\text{B}}$ to $(u_i, v_i)^{\text{true}}$ with $i = 1, \ldots, N$.

We repeated steps (d) to (h) for 50 noise trials and measured the mean and standard deviation of d_i^A and d_i^B with $i = 1, \ldots, N$. The resulting mean and standard deviation of d_i^A and d_i^B with $i = 1, \ldots, N$ at four different views are summarized in Table 1. Note that Table 1 only shows the result for balls that are visible in all considered views.

As shown in Table 1, the direct use of $\mathbf{P}$ results in less error than the indirect counterpart (which relies on geometric parameters decomposed from $\mathbf{P}$).

To further validate this fact, we conducted the following experiment. We illuminated the calibration phantom in the real scanner and acquired the projection data. From the projection data and the given geometry of the phantom, we performed geometric calibration and calculated the projection matrix $\mathbf{P}$. From $\mathbf{P}$, we decomposed to get $\mathbf{R}$, $\mathbf{K}$, $\mathbf{t}$. The actual geometric parameters were then calculated from $\mathbf{R}$, $\mathbf{K}$, $\mathbf{t}$.

After getting the geometric parameters from the real projection data, we performed forward projection in the software simulation with the calculated geometric parameters and compared the simulated projection image with the real one. In this case, the software calibration phantom was modeled identically to the real calibration phantom (ball sizes, shapes, and distribution of balls in the plastic holder). In particular, it was defined on a 3-D volume with a resolution of $1024 \times 1024 \times 1024$ and a voxel with a size of $(0.125 \text{ mm})^3$. Since the projection matrix relates the object coordinate and detector coordinate via two lists (x_i, y_i, z_i) and (u_i, v_i) with $i = 1, \ldots, N$, the origin of the object coordinate is set by (x_i, y_i, z_i). To match the software phantom with the real phantom, the list (x_i, y_i, z_i) with $i = 1, \ldots, N$ in the software phantom needs to match the one in the real phantom. In our software simulator, we have the means to define the position of the phantom and to move the phantom around to make its (x_i, y_i, z_i) list with $i = 1, \ldots, N$ match with the real phantom.

We repeated the above experiment with different projection views, and show representative results in Fig. 6. According to the results in Fig. 6, there are misalignments between the real projection images and the software-generated projection images. The differences become larger for balls far from the x-ray source.

Figure 7 shows the variation of α (where α is the angle formed by two axes of the detector bin) and the distance f between the source and detector in different views. As shown in Fig. 7, the extracted geometric parameters had unrealistic values, such as α varying (when it should not vary) and f changing too much in each view. We can observe that the degradations due to the approximations in decomposition and extraction (from $\mathbf{P}$ to geometric parameters) techniques are inevitable.

One can also consider adjusting the geometric parameters (for example, forcing $\alpha = 90$ deg) to make them close to the actual values provided by the manufacturer when setting up the system. Unfortunately, the new projection matrix generated by the corrected geometric parameters is different

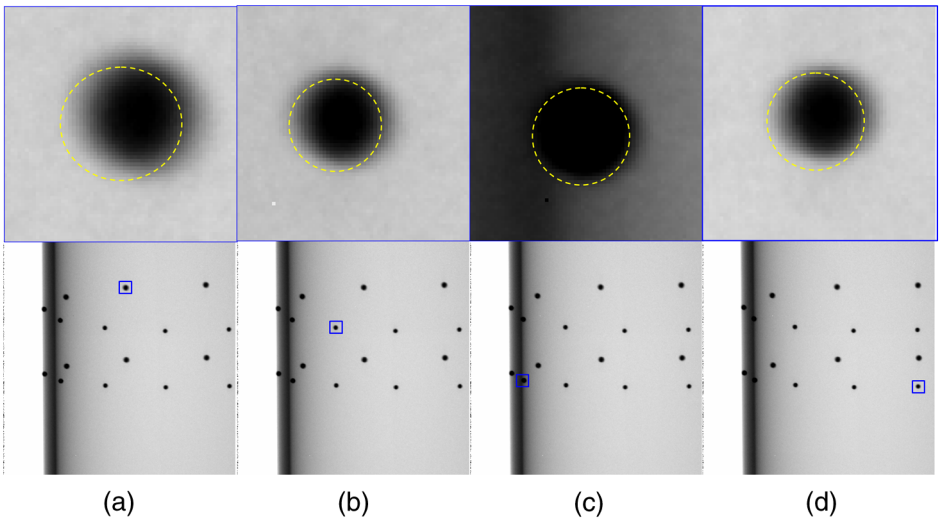

Fig. 6 Illustration of the errors due to the decomposition of the projection matrix into actual geometric parameters. (a)–(d) Projection images in different projection views. First row: the real projection image. Blue rectangles in first row denote the region to be zoomed in, shown in top row. Top row: zoomed-in region of the real projection image. The superposed dashed yellow circles denote the boundary of the balls in the projection image generated by the software simulator with geometric parameters estimated from the first row. (see description in the main text for details).

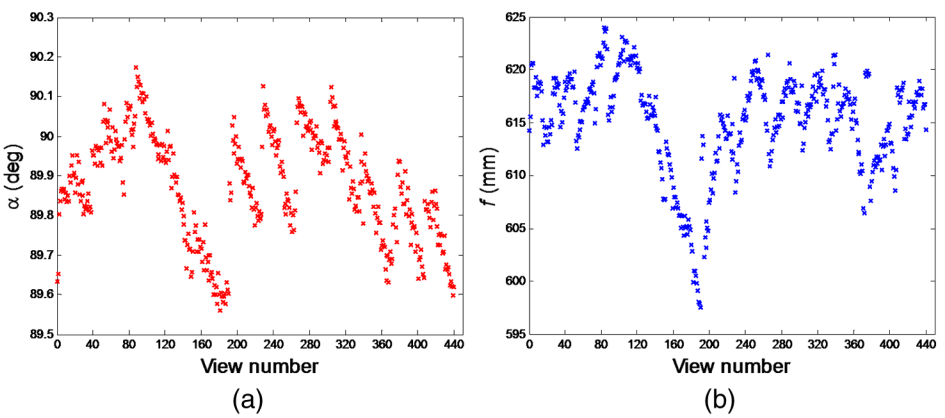

Fig. 7 Variation of estimated geometric parameters in a complete acquisition with 441 projection views: (a) the angle formed by two axes of detector elements and (b) distance from source to detector.

from the initially estimated one. Those differences result in errors in projection and backprojection operations. Therefore, the adjusted geometric parameters cannot be used in reconstruction.

To prevent numerical errors due to the abovementioned issues, we propose to directly use the projection matrix $\mathbf{P}$ and its pseudo-inverse matrix $\mathbf{P}^{\dagger}$ in reconstruction without going into the geometric parameters. The use of the projection matrix $\mathbf{P}$ and its pseudo-inverse $\mathbf{P}^{\dagger}$ in reconstruction will be addressed in the next subsection.

2.4 *Projection Matrix in Reconstruction Algorithms*

The geometric parameters define the system matrix, which is used in many iterative reconstruction methods.[16–20] In particular, the geometric parameters are used to construct the system matrix, which is key in performing projection and backprojection operations. In this paper, we consider the relaxed ordered-subset convex (OSC) algorithm,[17] which is a widely used algorithm in the field due to its advantage in providing high-quality reconstruction. In this section, the use of the projection matrix and geometric parameters in constructing a system matrix of the imaging system is presented.

The update equation of the OSC algorithm can be written as follows:

$$\mu_j^{(n,m+1)} = \mu_j^{(n,m)} + \lambda \mu_j^{(n,m)} \frac{\sum_{i \in S(m)} a_{ij}(\bar{p}_i - p_i)}{\sum_{i \in S(m)} a_{ij} \bar{p}_i g_i}, \quad \forall\, j, \qquad (4)$$

where $g_i = \sum_j a_{ij} \mu_j^{(n,m)}$, $\bar{p}_i = b_i \exp(-g_i)$; μ is the attenuation coefficient map (the image) to be reconstructed; a_{ij} denotes the element of the system matrix, which weights the contribution of the voxel indexed by j to the detector bin indexed by i; $\bar{p}_i$ is the expected number of transmission counts in detector element i; n is the iteration number; m is the subset number; λ is the relaxation parameter; p_i is the measured number of transmission counts in detector

element i; b_i denotes the blank scan counts in the i'th bin; and $S(m)$ contains the projection in subset m.

Element of system matrix a_{ij} is modeled by the intersecting chord length of the voxel j with the ray i, which is defined by the line connecting the x-ray source and the center of detector bin i.[21,22] To measure a_{ij}, we need to know the two end points of the line i. These two end points are indicated by the geometric parameters measured in Sec. 2.1. In particular, once the projection matrix $\mathbf{P}$ is computed, the source position $\mathbf{c}$ can be calculated by solving the equations $\mathbf{Pc} = \mathbf{0}$. The resulting $\mathbf{c}$ is given by $\mathbf{c} = (X_1/T_1, Y_1/T_1, Z_1/T_1)$:[12]

$$X_1 = \det([\mathbf{p}_1, \mathbf{p}_2, \mathbf{p}_3]), \quad Y_1 = -\det([\mathbf{p}_0, \mathbf{p}_2, \mathbf{p}_3]),$$
$$Z_1 = \det([\mathbf{p}_0, \mathbf{p}_1, \mathbf{p}_3]), \quad T_1 = -\det([\mathbf{p}_0, \mathbf{p}_1, \mathbf{p}_2]),$$

where $\mathbf{p}_0$, $\mathbf{p}_1$, $\mathbf{p}_2$, $\mathbf{p}_3$ are column vectors of $\mathbf{P}$, $\mathbf{P} = [\mathbf{p}_0\, \mathbf{p}_1\, \mathbf{p}_2\, \mathbf{p}_3]$. $\mathbf{c}$ is one end point of the ray i. The other end point of the ray i is at $(x, y, z) = (X_2/T_2, Y_2/T_2, Z_2/T_2)$, where X_2, Y_2, Z_2, T_2 are calculated as follows:

$$[X_2, Y_2, Z_2, T_2]^T = \mathbf{P}^{\dagger}[u, v, 1]^T, \tag{5}$$

where (u, v) is the coordinate of center of detector bin i in the detector space and $\mathbf{P}^{\dagger}$ is a 4×3 pseudo (right) inverse of $\mathbf{P}$, which is given by

$$\mathbf{P}^{\dagger} = \mathbf{P}^T(\mathbf{P}\mathbf{P}^T)^{-1}. \tag{6}$$

If one uses geometrical parameters (distance from source to detector f, the width p_u and the height p_v of detector bins, the angle α between two axes of the detector, the coordinate u_0, v_0 of interesting point of the central ray and the detector, rotation matrix $\mathbf{R}$, translation vector $\mathbf{t}$), the source position is given by $\mathbf{c} = -\mathbf{R}^T\mathbf{t}$. The other end point of the ray i is indicated by determining the object coordinate of the center

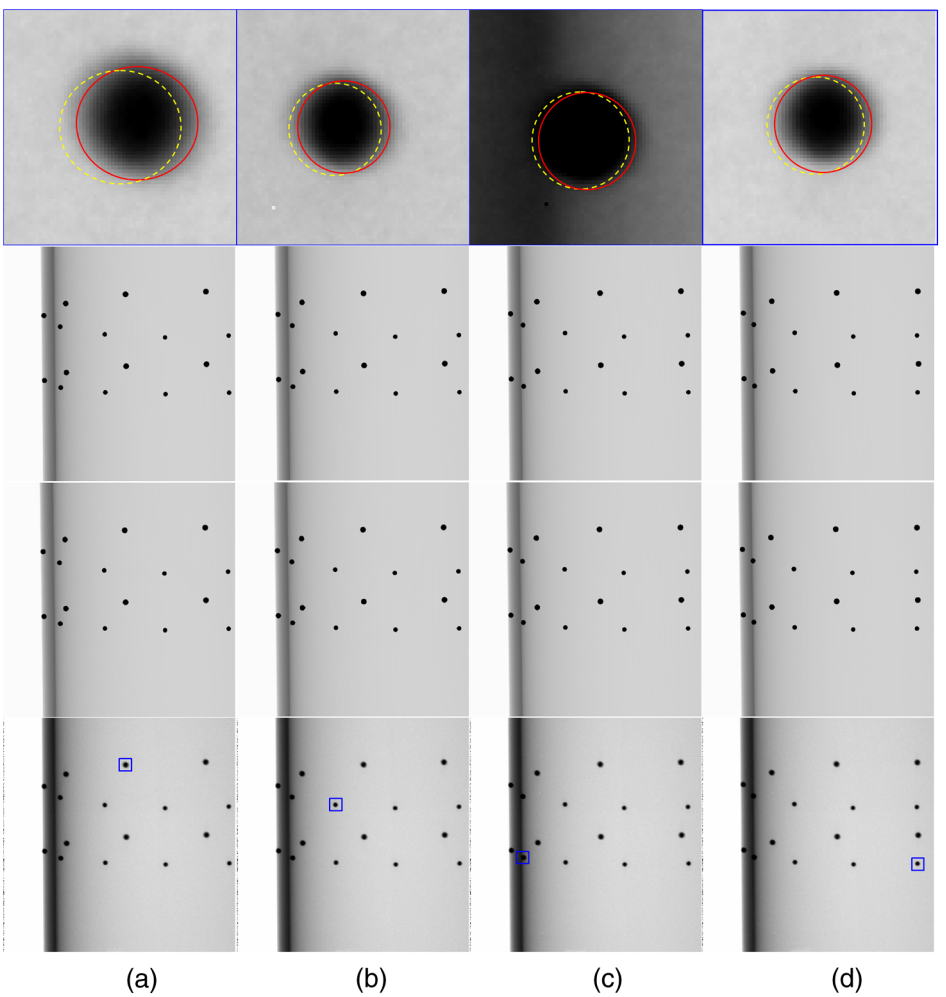

Fig. 8 Projection images acquired from scanner (using real calibration phantom) and projection images generated from software simulator using software calibration phantom with projection matrix and geometric parameters estimated from real data: (a)–(d) projection images in different projection views. First to third rows: real data, simulated data using method B, simulated data using method A. Blue rectangles in first row denote the region to be zoomed in, shown in top row. Top row: zoomed-in region of the real data. The superposed circles in the top row are the edges of software simulated projection data where solid red and dashed yellow circles denote the boundaries resulting from new method A and conventional method B.

of detector bin i as follows: $[x, y, z]^T = \mathbf{R}^{-1}(\mathbf{d} - \mathbf{t})$, where $\mathbf{d} = [u - u_0, v - v_0, f]^T$ and (u, v) is the coordinate of the center of detector bin i in detector space.

In practice, the projection matrix and its pseudo-inverse are precalculated before going into reconstruction. The use of the projection matrix and its pseudo-inverse does not result in more computation time, since: (i) only two matrix multiplications are required to determine end-points of the ray i in the projection; (ii) only one matrix multiplication to determine the detector bins contributes to considering voxel j in the backprojection (if the voxel-driven backprojection method[22] is used). These computations are on par with those in the conventional method, which directly uses geometric parameters.

3 Results

To evaluate the performance of the proposed method, we performed the experiment with a real scanner. The offset flat-panel CBCT system used in this work was a Papaya 3D™ scanner from Genoray Co., Ltd., South Korea. The detector of the scanner had a size of 128.6 mm × 130.5 mm. The detector bin size was (0.1 mm × 0.1 mm), which gives the detector a resolution of 1286 × 1305. Other parameters were determined from the calibration process. The calibration phantom was manually made with the specifications given in Sec. 2.2. A software version of the calibration phantom was also generated accordingly.

The calibration phantom was illuminated using the real CBCT scanner to generate projection data. The new calibration method was applied to the acquired projection data to estimate the projection matrix. The estimated projection matrix and its inverse were then used to perform projections in the software simulator with the software calibration phantom (using the ray-tracing[21] method with the value of a blank scan set to $b = 4095$). Finally, the estimated projection matrix and its inverse were used to reconstruct the image from a real dataset. This method is denoted as "method A."

We also performed calibration using the conventional method (with decomposition of $\mathbf{P}$ to $\mathbf{K}$, $\mathbf{R}$, $\mathbf{t}$ followed by extraction) to get the geometric parameters. The estimated geometric parameters were used to model the system matrix in the projection and backprojection operations. This method is denoted as "method B."

Figure 8 shows the projection images of the calibration phantom acquired from the scanner and the ones generated from the software simulator with the projection matrix (method A) and geometric parameters (method B) estimated from the acquired projection image. Note that while the acquired projection image was contaminated by Poisson noise in the acquisition process, the simulated one was a noiseless image. As shown in Fig. 8 (especially the top

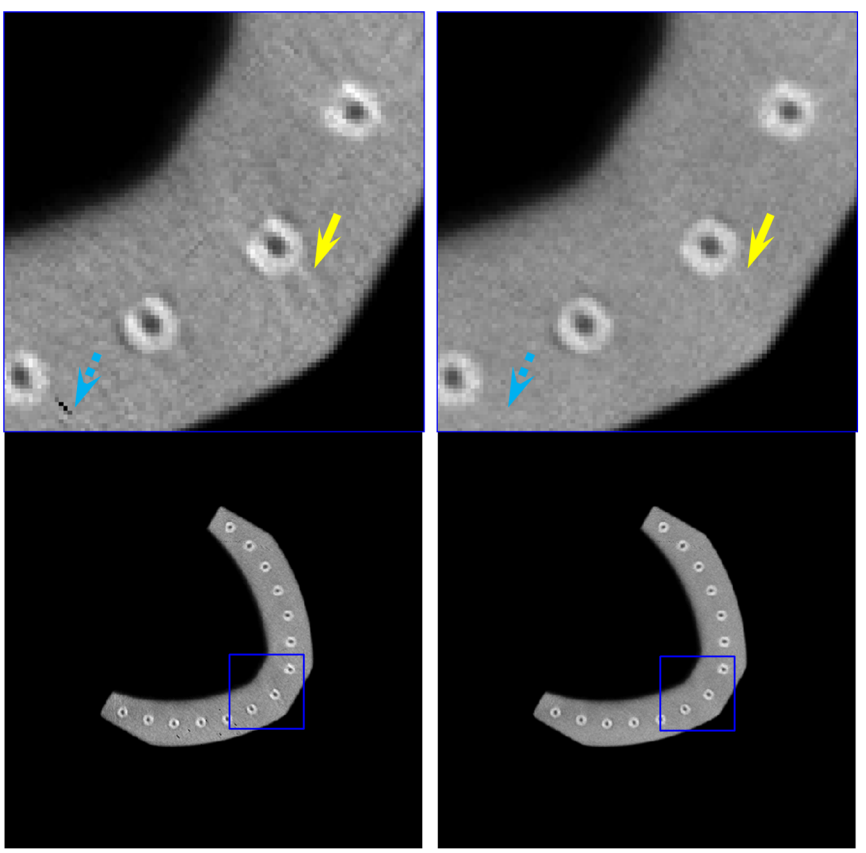

Fig. 9 OSC reconstructions from real data of arch phantom using: (a) method B and (b) method A. First row: axial slices. Second row: zoomed-in region of (a). The arrows indicate the area of artifacts due to incorrect geometric parameters in conventional method.

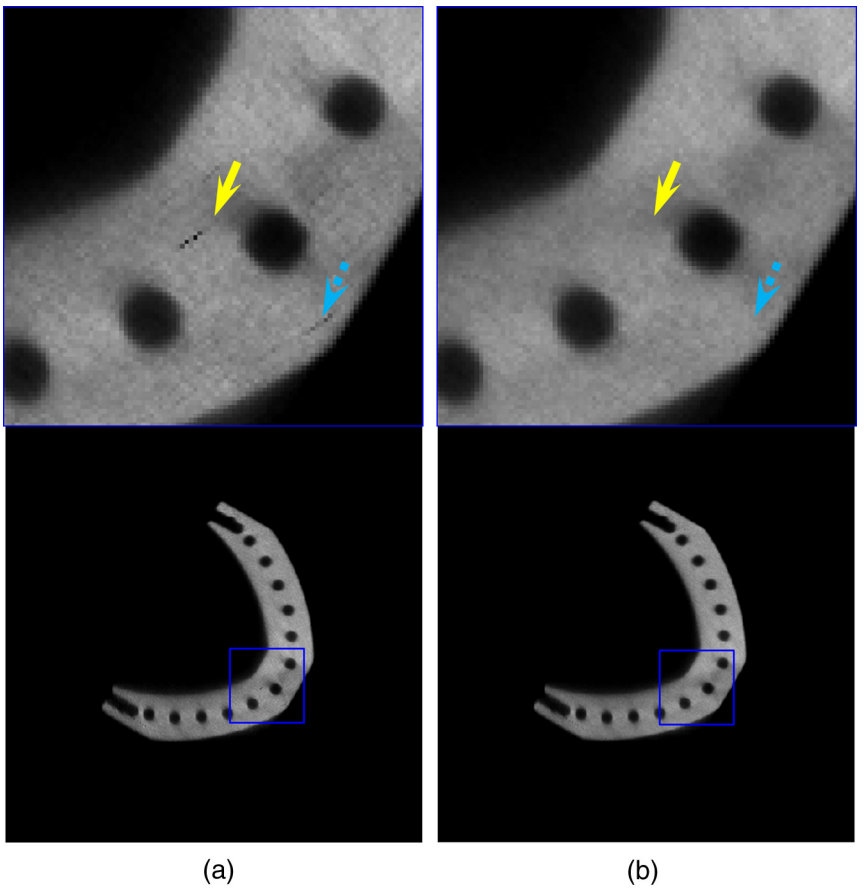

Fig. 10 Same as Fig. 9 but in a different slice. (a) Method B and (b) method A.

row), the projection image generated by the new method A achieves almost identical results in comparison with the real projection image (see solid red boundary in top row), whereas the one generated by method B deviates from the real one.

Using the projection matrix and geometric parameters estimated above, we performed the reconstruction with a real dataset acquired from an arch phantom. The OSC algorithm was used to reconstruct images.

According to the results in Fig. 9, the new method overcomes the limitations of the conventional method and results in more accurate results [see Fig. 9(b)] and fewer artifacts [see arrows in Figs. 9(a) and 9(b)]. Without decomposing **P** into geometric parameters, the new method A prevents the streak artifacts that appear in the conventional method. Furthermore, it also reduces unwanted artifacts due to degraded detector cells in the detector. This fact is also clearly shown in Fig. 10, where the proposed method A results in fewer artifacts than the conventional geometric calibration method.

4 Conclusions

We have developed a new calibration method for offset flat-panel CBCT systems, which can accurately determine the geometric parameters for each projection view. The new method comes with a calibration phantom specially designed for offset flat-panel CBCT scanners. We have generalized the projection matrix method to offset flat-panel CBCT scanners without major changes to the calibration process. We have also introduced the use of the pseudo-inverse of the projection matrix and projection matrix for projection and backprojection operations. By using the projection matrix and its pseudo-inverse (not decomposing the projection matrix into geometric parameters as in previous works), we prevent numerical errors due to preset constraints on the geometric parameters and approximations in decomposition that might cause degradation in projection and backprojection operations and thereby reconstruction. The proposed method was validated with software data and real data experiments, where it provides more accurate results than the conventional methods.

In conclusion, the proposed method uses an accurate geometric calibration technique in real-world situations where the scanner is unstable and geometric parameters are view dependent. The new method improves the quality of reconstruction and frees CT makers and practitioners from time-consuming calibration work for offset flat-panel CBCT systems.

Acknowledgments

This research was funded by Vietnam National Foundation for Science and Technology Development (NAFOSTED) under Grant No. 102.01-2013.42.

References

1. J. Hsieh, *Computed Tomography: Principles, Design, Artifacts, and Recent Advances*, 2nd ed., SPIE Press, Bellingham, Washington (2009).
2. J. F. Barrett and N. Keat, "Artifacts in CT: recognition and avoidance," *Radiographics* **24**(6), 1679–1691 (2004).

3. Y. Cho et al., "Accurate technique for complete geometric calibration of cone-beam computed tomography systems," *Med. Phys.* **32**(4), 968–983 (2005).
4. X. Li, D. Zhang, and B. Liu, "A generic geometric calibration method for tomographic imaging systems with flat-panel detectors—a detailed implementation guide," *Med. Phys.* **37**(7), 3844–3854 (2010).
5. A. Ladikos and W. Wein, "Geometric calibration using bundle adjustment for cone-beam computed tomography devices," *Proc. SPIE* **8313**, 83132T (2012).
6. D. Panetta et al., "An optimization- based method for geometrical calibration in cone-beam CT without dedicated phantoms," *Phys. Med. Biol.* **53**(14), 3841–3861 (2008).
7. I. Tekaya et al., "Registration-based geometric calibration of industrial x-ray tomography system," *IEEE Trans. Nucl. Sci.* **60**(5), 3937–3944 (2013).
8. J. Muders, Geometrical Calibration and Filter Optimization for Cone-Beam Computed Tomography, PhD Dissertation, Heidelberg University (2015).
9. Y. Meng, H. Gong, and X. Yang, "On-line geometric calibration of cone-beam computed tomography for arbitrary imaging objects," *IEEE Trans. Med. Imaging* **32**(2), 278–288 (2013).
10. Y. Kyriakou et al., "Simultaneous misalignment correction for approximate circular cone-beam computed tomography," *Phys. Med. Biol.* **53**(22), 6267–6289 (2008).
11. J. Wicklein et al., "Image features for misalignment correction in medical flat-detector CT," *Med. Phys.* **39**(8), 4918–4931 (2012).
12. R. Hartley and A. Zisserman, *Multiple View Geometry in Computer Vision*, 2nd ed, Cambridge University Press, Cambridge, United Kingdom (2004).
13. J. Nocedal and S. Wright, *Numerical Optimization*, Springer, New York City (2006).
14. E. Hansis et al., "Iterative reconstruction for circular cone-beam CT with an offset flat-panel detector," in *Proc. IEEE NSS-MIC*, pp. 2228–2231 (2010).
15. G. Wang, "X-ray micro-CT with a displaced detector array," *Med. Phys.* **29**(7), 1634–1636 (2002).
16. H. Erdogan and J. A. Fessler, "Ordered subsets algorithms for transmission tomography," *Phys. Med. Biol.* **44**, 2835–2851 (1999).
17. J. S. Kole and F. J. Beekman, "Evaluation of the ordered subset convex algorithm for cone-beam CT," *Phys. Med. Biol.* **50**, 613–623 (2005).
18. J.-B. Thibault et al., "A three-dimensional statistical approach to improved image quality for multislice helical CT," *Med. Phys.* **34**(11), 4526–4544 (2007).
19. J. Hsieh et al., "Recent advances in CT image reconstruction," *Curr. Radiol. Rep.* **1**(1), 39–51 (2013).
20. J. Bian et al., "Optimization-based image reconstruction from sparse-view data in offset-detector CBCT," *Phys. Med. Biol.* **58**(2), 205–230 (2012).
21. R. L. Siddon, "Fast calculation of the exact radiological path for a three dimensional CT array," *Med. Phys.* **12**(2), 252–255 (1985).
22. V. G. Nguyen and S. J. Lee, "Parallelizing a matched pair of ray-tracing projector and backprojector for iterative cone-beam CT reconstruction," *IEEE Trans. Nucl. Sci.* **62**(1), 171–181 (2015).

Van-Giang Nguyen received his BS degree in computer science from Le Quy Don Technical University (a.k.a. Military Technical Academy), Hanoi, Vietnam, in 2005, and his MSc and PhD degrees in electronic engineering from Paichai University, Daejeon, Korea, in 2009 and 2012, respectively. Since 2013, he has been with the Department of Information Systems, Le Quy Don Technical University, Hanoi, Vietnam. His current research interests include image processing, computer vision, and their applications to medical physics and tomographic reconstruction.